Up-Conversion Imaging Processing With Field-of-View and Edge Enhancement

Shi-Kai Liu,[1,2] Chen Yang,[1,2] Shi-Long Liu,[1,2] Zhi-Yuan Zhou,[1,2,3,*] Yan Li,[1,2] Yin-Hai Li,[1,2,3] Zhao-Huai Xu,[1,2] Guang-Can Guo,[1,2] and Bao-Sen Shi[1,2,3,†]

[1] *CAS Key Laboratory of Quantum Information, University of Science and Technology of China, Hefei, Anhui 230026, China*
[2] *Synergetic Innovation Center of Quantum Information & Quantum Physics, University of Science and Technology of China, Hefei, Anhui 230026, China*
[3] *Wang Da-Heng Collaborative Innovation Center for Science of Quantum Manipulation & Control, Heilongjiang Province & Harbin University of Science and Technology, Harbin 150080, China*

(Received 6 October 2018; revised manuscript received 12 February 2019; published 4 April 2019)

Spiral phase contrast (SPC) is an important and commonly used image processing technology in edge detection applications, and realization of a broader field-of-view (FOV) is a long-pursued aim in imaging systems to allow more regions of the illuminated objects to be observed. Using the image processing technologies described, we first acquire both an enhanced FOV and SPC images using second-order nonlinear frequency up-conversion from the near-infrared (NIR) spectrum to the visible spectrum in two different configurations. In addition, SPC operation and sum-frequency generation using two different wavelengths is performed simultaneously within a periodically poled potassium titanyl phosphate (PPKTP) crystal by applying a vortex filter to the pump beam. When compared with the NIR spectrum, the up-converted image in the visible spectrum benefits from the advantages of higher detection sensitivity and lower potential speckle. By optimizing the temperature of the PPKTP crystal, controllable spatial patterns of up-converted images with observation cone angle enhancement of the FOV by more than 2.1 times is realized in both configurations. Additionally, we perform numerical simulations of the above phenomenon and the results agree well with those of the experimental observations. Our results provide a very promising image processing method that may be widely used in biomedicine and up-conversion monitoring applications.

DOI: 10.1103/PhysRevApplied.11.044013

I. INTRODUCTION

Optical imaging systems using near-infrared (NIR) illumination have a wide range of applications including biomedicine, surveillance, and military systems [1–3]. The wavelength range around 1550 nm is of specific interest for LIDAR imaging systems because of several advantages, including the fact that it is an eye-safe spectral region, it shows good atmospheric transparency, and high-peak power lasers are available in this range [4]. However, CCDs in this spectral domain, which are commonly based on InGaAs materials, suffer from reduced efficiency and speed, high readout noise, and more rigorous cooling attachment requirements than silicon CCDs in the visible range. Existing infrared detection technology has thus limited the development of direct infrared imaging processes. Therefore, it is necessary to convert the infrared illumination to the visible spectrum [5,6]. Up-conversion detection based on sum-frequency generation (SFG), which is a second-order nonlinear optical process, can visualize infrared images using standard silicon CCDs, thus helping to improve imaging performance and sensitivity. Two additional important aspects of a typical imaging processing method that must be considered are edge and field-of-view (FOV) enhancement.

Phase contrast in imaging dates back to the initial prominent work performed by Frits Zernike on edge detection in the 1930s [7], in which he presented a new method for microscopic observation of transparent objects. In optical imaging systems, the spiral phase contrast (SPC) technique has been developed to increase the contrast of intensity and phase objects using a vortex structure filter [8]. In 2005, Jesacher *et al*. realized an oriented shadow effect for SPC imaging of a human cheek cell using a modified spiral phase hologram [9]. Fractional vortex filters were also investigated to obtain gradual edge enhancement by Chen *et al*. in 2015 [10]. SPC is not just limited to the classical region and can also be translated into the quantum world. In 2009, SPC ghost imaging using correlated photon pairs was proposed based on placement of a vortex phase plate (VPP) in one arm of the imaging system, which then allows edge enhancement to occur in another arm of the system [11]. This technique is based

*zyzhouphy@ustc.edu.cn
†drshi@ustc.edu.cn

on processing of the image spectral information of phase or amplitude objects in the Fourier plane of a 4 focus length (4-f) imaging system using a helical phase mask as a spatial filter with a topological charge of $L = 1$. Spiral operation manipulates the phase of the entire light field in the form of a spiral-shaped phase profile of the form $e^{i\varphi}$, where φ is the polar angle in a plane transverse to the light propagation direction [12]. On account of the odd symmetry of the spiral phase, both the phase and amplitude gradients can be enhanced isotropically. SPC imaging is widely applied in microscopic imaging systems using visible light for contrast enhancement. Additionally, SPC imaging may have potential applications including two-dimensional (2D) infrared spectroscopy detection [13], gas leak sensing [14], infrared monitoring in the military domain [15], and biological imaging [16], in which the use of infrared illumination is generally preferred. However, image detection in the infrared region has certain limitations and disadvantages when compared with detection in the visible regime. It is thus wise to up-convert the infrared image into the visible regime for higher detection sensitivity and efficiency. By combining SPC operation with an SFG process, both edge enhancement and frequency up-conversion of the invisible objective image can be observed simultaneously by loading the helical phase structure into the pump beam and using a periodically poled potassium titanyl phosphate (PPKTP) crystal as a nonlinear SPC filter between the lenses of the 4-f set up; this interesting setup is highlighted in our experiment in configuration *B*. This achievement may provide a fascinating and alternative method for up-conversion edge detection in the infrared illumination regime that will also have all the original merits of short-wavelength detection and will also provide an interface between the different light frequencies.

In addition, we have discovered a phenomenon where the FOV of the up-converted image can be enhanced during temperature changes in the PPKTP crystal. The traditional methods for increasing the FOV are generally realized using a broad bandwidth pump laser [17], dual illumination wavelengths [18], an amplified spontaneous emission (ASE) illumination source [6], crystal rotation [19], and a designed temperature gradient inside the crystal [20]. All of these methods aim to satisfy the phase matching conditions for different incident signal angles. In contrast to the state-of-the-art approaches above, we demonstrate a very convenient and simple method that places no demands or limitations on specially required devices such as laser sources and complex temperature gradient controllers and has no need for precise crystal rotation, which may cause slight image intensity and position variations. All that is required is to optimize the temperature of the nonlinear crystal, while all the experimental set ups remain the same. The converted observation cone angle is used to fully describe the absolute FOV enhancement of the image; the enhancement is given by the square root of the area enhancement factor and area (observation cone angle) enhancement of more than 4.5 (2.1) times is achieved using two narrowband lasers. Furthermore, temperature optimization offers a particularly simple way to experimentally implement the proposed method. We believe this is the first time that this method has been carried out and it will have a wide range of useful applications because of its minimal experimental set-up requirements. It should also be mentioned that the same FOV enhancement phenomenon can be produced by varying the wavelength of the pump beam or the illumination beam while maintaining the crystal at a constant temperature, thus providing an alternative way to realize this effect. The experimental and simulated results show nonintegrated images obtained at different temperatures with the aim of realizing high-speed real-time imaging applications.

Recent work in up-conversion SPC imaging with frequency doubling at 1064 nm using a type-II KTP crystal based on critical phase-matching was experimentally achieved by Chen's group [21]. This was the first time that the SPC imaging technique was realized in a nonlinear optical process. However, their configuration can only convert the specific given wavelength of 1064 nm with no walk-off effect, which limits the wavelength tunability. In contrast, the advantage of our up-conversion configuration using a type-I PPKTP crystal based on quasi-phase-matching (QPM) is that the largest nonlinear coefficient (d_{33}) can be used and no walk-off effect occurs at the same time [22]. Therefore, the conversion efficiency will be higher than that of a KTP crystal in terms of critical phase matching with a higher effective nonlinear coefficient. Additionally, we can obtain up-conversion imaging at any arbitrary wavelength by appropriate design of the QPM periods of the crystal and the coating. To date, our work represents the first time that up-conversion SPC imaging has been achieved using a vortex pump beam at a different wavelength to the imaging beam with FOV enhancement occurring simultaneously and thus can present some alternative experimental opportunities for multiwaveband imaging.

II. THEORETICAL MODEL AND SIMULATIONS

Standard SPC theory is used to produce configuration *A* (Fig. 2), which is first introduced to provide a better understanding of the nonlinear SPC below. The generic set up used for Fourier filtering is a 4-f system with two lenses designated $L1$ and $L2$, as shown in Fig. 2. $E_s(r,\phi)$ is the input object's light field, while its spatial Fourier spectrum is $E_s(\rho,\varphi) = \mathcal{F}[E_s(r,\phi)]$. A SPC filter is placed on the back spectrum of lens $L1$ and its transmission function is given by $F(\rho,\varphi) = \mathrm{circ}(\rho/R)\exp(i\varphi)$, where R is the aperture radius of $\mathrm{circ}(\rho/R)$. The entire light field in the

Fourier plane is

$$E_f(\rho,\varphi) = F(\rho,\varphi) \times \mathcal{F}[E_s(r,\phi)], \tag{1}$$

where $\times$ represents the dot product operation and $\mathcal{F}$ denotes the Fourier transform. After lens $L2$ "undoes" the Fourier transform, the final filtered image in the image plane is given by

$$E_c(r,\varphi) = \mathcal{F}[F(\rho,\varphi)] * E_s(r,\phi), \tag{2}$$

where * represents a convolution. The point spread function, which is expressed as $K(r,\varphi) = \mathcal{F}[F(\rho,\varphi)]$, is the Fourier transform of the spiral phase filter, which is a diffraction-limited doughnut-shaped intensity ring with a helical phase of between 0 and 2π around the ring. When the convolution calculation is performed, every single point in the image is weighted using the point spread function. In "flat" regions, every adjacent point has a constant phase or amplitude distribution, leading to signal cancellation because of the phase difference of π between any two points across the center of the doughnut [12]. In contrast, at the "edges" of the structures, at which the amplitude or phase gradients occur, the cancellation process is not perfect, which leads to a signal being generated. Then, the integration is carried out over the entire illuminated part of the resolution target, which leads to the edge enhancement effect for the whole image.

In configuration B, the SPC operation is a second-order nonlinear filtering process based on SFG that uses a short PPKTP crystal as a nonlinear filter for a vortex pump beam carrying orbital angular momentum (OAM), thus enabling up-converted visible edge detection with invisible illumination. The nonlinear interaction occurs at the Fourier spectrum plane of the 4-f system in which the crystal is positioned. Intriguingly, this approach makes the two steps of standard SPC and the up-conversion process in configuration A into a single process, which is first introduced to be applied to up-conversion edge detection with the SFG process using 1556-nm eye-safe illumination. This is the main difference when compared with the standard linear SPC operation shown in configuration A. The PPKTP crystal plays a crucial role in multiplying the OAM and the object information together to achieve edge enhancement of the up-converted SPC image in a single step by imaging the vortex filter on the nonlinear crystal. The Fourier transform of the object that is illuminated using the NIR beam with wavelength λ_s is $E_s(\rho,\varphi,\lambda_s) = \mathcal{F}[E_s(r,\phi,\lambda_s)]$. The output SFG light field at the focal plane of lens 3 ($L3$) is governed by the wave coupling equation shown as Eq. (3) and it is simplified using the paraxial approximation and slowly varying amplitude field approximation

$$\frac{\partial E_c(\rho,\varphi,\lambda_c)}{\partial z} = \frac{2i\omega_c^2 d_{\text{eff}}}{k_c c^2} E_s(\rho,\varphi,\lambda_s) F_p(\rho,\varphi,\lambda_p) e^{-i\Delta kz} + \frac{i}{2k_c}\Delta E_c(\rho,\varphi,\lambda_c). \tag{3}$$

Here, λ_c is the wavelength of the converted SFG beam, λ_p is the wavelength of the pump beam, d_{eff} is the effective nonlinear coefficient, and c is the speed of light in vacuum. After the linear term of Eq. (3) is abandoned using the plane wave approximation, we obtain the wave coupling equation in a simplified form as

$$\frac{\partial E_c}{\partial z} = \frac{2i\omega_c^2 d_{\text{eff}}}{k_c c^2} E_s F_p e^{-i\Delta kz}. \tag{4}$$

Under the optimal phase matching condition where $\Delta k = 0$, the output image on the imaging plane of the nonlinear 4-f system can be expressed as

$$E_c(r,\phi,\lambda_c) \propto E_s(r,\phi,\lambda_s) * \mathcal{F}[F_p(r,\phi,\lambda_p)] \tag{5}$$

where $*$ represents the convolution operation, and the invisible signal is converted into the visible output SPC image by imprinting the vortex filter on the nonlinear crystal [21]. According to the wave coupling equation, the spiral phase structure of the form $e^{i\varphi}$ is transferred from the pump beam to the conversion beam during the overall process and this structure will modify every single point on the Fourier spectrum of the input image via a nonlinear interaction, shifting the relative phase and frequency of the input image to the corresponding quantities of the up-converted image between the two points across the center of the donut-shaped structure. Therefore, the Fourier filtered image will block out all light from the flat inner regions and highlight the edge profile.

The FOV is a fundamental parameter of an imaging system and ways to improve the FOV have long been sought. The FOV is like an adjustable aperture with a size that is dictated by the noncollinear phase matching condition of the up-conversion process in Fourier space. In our case, the QPM condition's dependence on temperature is expressed as

$$\Delta k = 2\pi\left(\frac{n_{\lambda_s}(T)}{\lambda_s} + \frac{n_{\lambda_p}(T)}{\lambda_p} - \frac{n_{\lambda_c}(T)}{\lambda_c} + \frac{1}{\Lambda(T)}\right),$$

where n represents the refractive index at the different wavelengths. When $\Delta k = 0$, this means that the momentum mismatch is fully compensated by the reciprocal vector of the QPM crystal. By changing the temperature of the PPKTP crystal, up-conversion controllable spatial patterns with different FOVs for the SHG beam can be observed. This phenomenon was first discovered by our group in

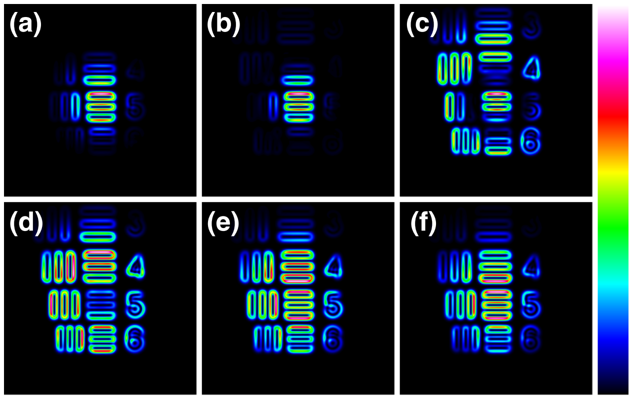

FIG. 1. Image simulation of edge and FOV enhancements of the USAF-1951 resolution target. The color bar is given on the right side.

2014 [23]. In Ref. [23], controllable spatial structures in the SFG light beam were reported that were achieved by crystal phase mismatching produced by tuning the pump frequency or the crystal temperature; two Gaussian pump beams were used in this process. In this work, we “add” image processing to this model and find that the FOV of the up-converted image can be tuned periodically, thus allowing more regions of the illuminated object to be seen.

Next, numerical simulation of the nonlinear imaging process, which combines FOV enhancement with SPC operation using configuration *B*, is performed. A computational numerical tool based on configuration *B* is developed to simulate the image processing for edge and FOV enhancement to allow us to anticipate the improvements that will be produced by the experimental set up and provide feedback to continue the optimization of the proposed up-conversion system. All the simulation parameters, including the crystal length, the beam waist, and focal length of the lenses, are in accordance with those used in the experimental set up.

In our simulation, we use the Collins diffraction integral equation and the split-step Fourier method to obtain the simulated output image from the nonlinear 4-f system shown in Fig. 1. We only show the main frame for the light evolution and propagation in the main text; for a detailed discussion with a step-by-step derivation of the formula during the nonlinear process, please refer to the Appendix. As the figure shows, the FOV and the spatial pattern of the image both change with the phase mismatching parameter of temperature and we obtain a theoretical FOV enhancement of 2.2 times based on the ratio of the maximum FOV [image (d), 12.3 mrad] to the minimum FOV [image (b), 5.6 mrad].

III. EXPERIMENTAL SET UP

The two different configurations used in our experimental set up are displayed in Fig. 2. First, configuration *A* is introduced as follows. We begin by generating an infrared SPC image using a standard SPC operation, and then use a Gaussian pump beam to up-convert this image to the visible regime. By changing the temperature of the PPKTP crystal, we achieve FOV-enhanced SPC imaging. The 1556.3-nm illumination beam is provided by a diode laser (prodesign, Toptica) and is amplified using an erbium-doped fiber amplifier. The pump beam at the wavelength of 791.8 nm is from a Ti:sapphire laser. Both beams are continuous narrowband waves and are fiber-coupled

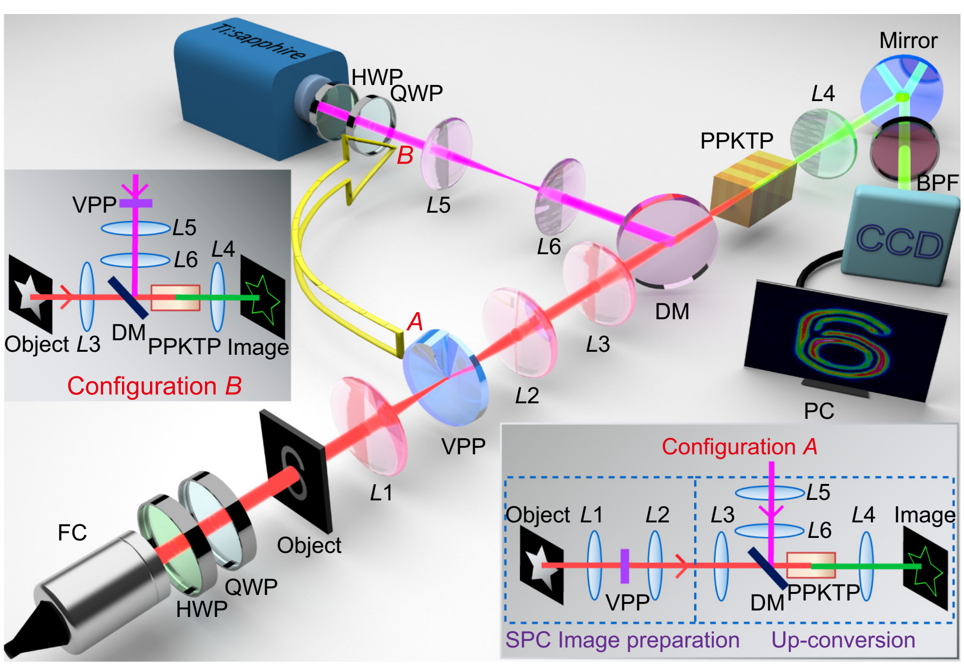

FIG. 2. Experimental set ups for up-conversion SPC imaging system showing two configurations. FC: fiber collimator; HWP: half-wave plate; QWP: quarter-wave plate; BPF: band-pass filter; DM: dichroic mirror; VPP: vortex phase plate; PC: personal computer; *L*1–*L*6: lenses.

using fiber collimators. The U.S. Air Force MIL-STD-150A standard of 1951 (USAF-1951) resolution target is then inserted as the illumination intensity object. Two pairs of half-wave plates (HWPs) and quarter-wave plates (QWPs) are used in each beam to optimize their polarization directions and then satisfy the type-I phase matching condition. The type-I PPKTP crystal that we use in our experiment is 3-mm long, with an aperture of 2×1 mm^2; both end faces are antireflection coated for 524.8, 1556.3, and 791.8 nm, and its quasiphase matching periodic poling period is 19.4 μm. The temperature of the PPKTP crystal is controlled using a homemade temperature controller with a stability of $\pm 0.002\,^{\circ}$C. Lens $L1$, lens $L2$, and the VPP with a topological charge of $L = 1$ that is inserted into the waist of the illumination beam are used to form an SPC 4-f imaging system. The topological charge of the VPP aligns with the center of the beam. Then, lens $L3$ focuses the SPC image into the PPKTP crystal. The pump beam is transformed into beams that are two times smaller in diameter by a 4-f system consisting of lens $L5$ and lens $L6$, which have confocal lengths of 300 and 150 mm, respectively. A dichroic mirror reflects the pump beam and translates the illumination beam such that they overlap in the same direction. The PPKTP crystal is positioned in the Fourier plane of the up-conversion 4-f system composed of lenses $L3$ and $L4$. The output image is cleaned up using a band-pass 525-nm filter with a full width at half maximum of 10 nm. Then, a low-noise and high-speed CCD (BC106-VIS, Thorlabs) records the visible converted image.

Configuration B is largely based on experimental set up A, but with a slight change. The VPP operating at 1556 nm is removed and inserted into the path of the pump beam at the position of the front focal plane of the 4-f system formed of lenses $L5$ and $L6$. Then, we switch the VPP to the wavelength of 792 nm and align it with the center of the pump beam. The image without SPC is generated using the first 4-f system that includes lenses $L1$ and $L2$. Next, the pump beam carrying the OAM light is mixed with the illumination beam and imprints the VPP on the PPKTP crystal during SFG. In this way, the up-conversion and SPC processes occur in a single step, which is simpler and more convenient.

IV. EXPERIMENTAL RESULTS

In the above configurations, three asymmetric Arabic numerals, 4, 5, and 6, are selected as intensity objects to show the universality of the objects. Up-converted images of the single numbers with and without SPC are acquired. The output images are shown in Fig. 3. Our experimental results agree well with those of the theory and the simulations. Through the SPC-based imaging process, we can see both the outline and the shapely edge enhancement in images (b1)–(b3) and images (c1)–(c3) in Fig. 3. When compared with the images acquired using configuration B,

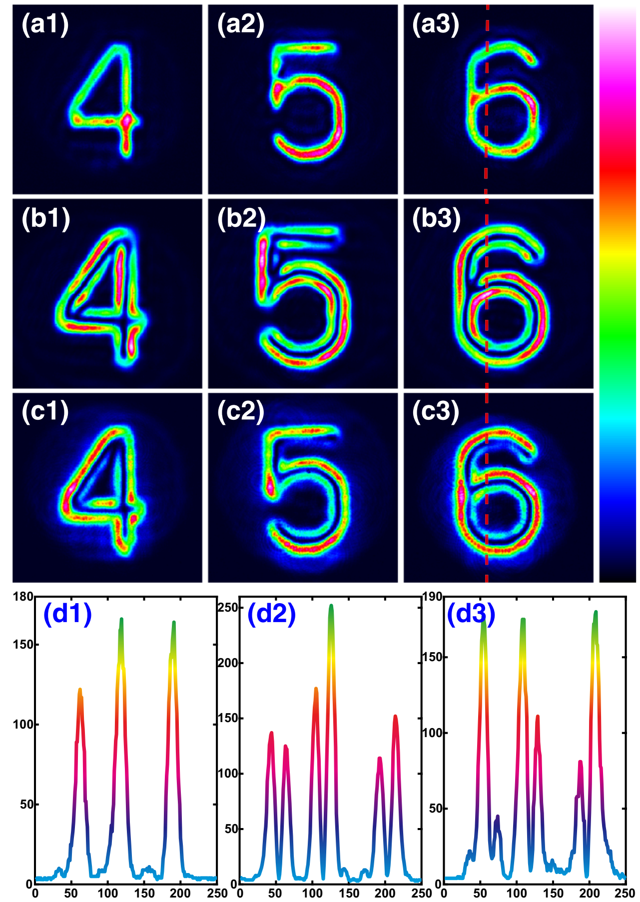

FIG. 3. Experimental up-conversion images of the numbers 4, 5, and 6. (a1)–(a3) are the images without SPC. (b1)–(b3) are the SPC images acquired using configuration B. (c1)–(c3) are the SPC images acquired using configuration A. The color bar is shown on the right side of the figure; all other figures below use the same color bar, so it will not be shown again. Line charts (d1)–(d3) correspond to the vertical intensity distributions of images (a3)–(c3), respectively.

more speckle and scattered noise can be seen in the images acquired using the other configurations because the NIR illumination beam suffers slight scattering at the focal plane where the VPP is positioned in the SPC 4-f system [24].

To perform an approximate analysis of the image quality, we define the average visibility as the index that is used to evaluate the quality of the SPC: $V = [(I_{\max} - I_{\min})/(I_{\max} + I_{\min})]$. Here, $I_{\max}$ is the average maximum gray value of the enhanced outlines, while $I_{\min}$ is the minimum gray value of the dark region between the highlighted outlines. Line charts (d1)–(d3) show the vertical intensity distribution results from images (a3) to (c3) along the direction of the red dashed line in Fig. 3, and the average visibilities for the two schemes in images (b3) and (c3) of the number 6 are approximately 91.8% and 77.7%, respectively, which show higher contrasts and

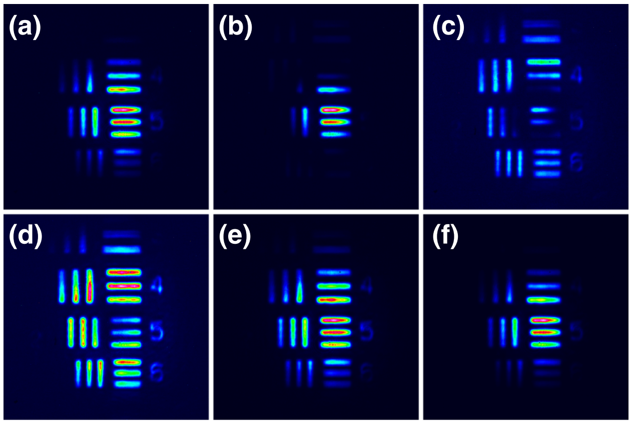

FIG. 4. The temperature-controllable FOVs of the image are shown in (a)–(f). The temperature conditions in images (a)–(f) are 18.7 °C, 29.6 °C, 33.0 °C, 34.5 °C, 37.1 °C, and 45.7 °C, respectively.

lower backscattered noise than that of the nonlinear SPC configuration.

Another area of the USAF-1951 resolution target is selected as an illumination object to demonstrate the improvement in the FOV. When we adjust the temperature of the PPKTP crystal, different FOVs are obtained for the converted images because of phase mismatching, as demonstrated in Fig. 4. The ratio of the maximum FOV [image (d), 10.1 mrad] to the minimum FOV [image (b), 4.0 mrad] is 2.5 times for the observation angle enhancement. This interesting process is much more like an "adjustable aperture" analogous to the different views that can be obtained by the wide-angle lens of a camera, in which different illuminated parts of the object are selectively imaged as the crystal's temperature changes. In addition, the quality and the contrast ratio of the image remain the same despite the changes in temperature.

Next, we discuss the imaging process that simultaneously provides both FOV and edge enhancement using two configurations. Figure 5 depicts all the outcomes of the up-conversion imaging process. Two different locations on the USAF-1951 resolution target are used as illumination parts for the two configurations. As is vividly illustrated by the images, the outline of the entire intensity object is highlighted with different spatial patterns by controlling the PPKTP crystal's temperature. In Fig. 5, the ratio of the maximum FOV [image (a4), 9.6 mrad] to the minimum FOV [image (a3), 4.5 mrad] is 2.1 times for the observation angle enhancement in configuration *A* and the ratio of the maximum FOV [image (b5), 10.0 mrad] to the minimum FOV [image (b3), 4.7 mrad] is 2.1 times for the observation angle enhancement in configuration *B*. In comparison, the image acquired using configuration *A* has a little stray light in the background due to focusing light diffraction on the filter. In general, the two configurations are basically equivalent in both theory and experiment, and only depend on which light beam arm carries the OAM.

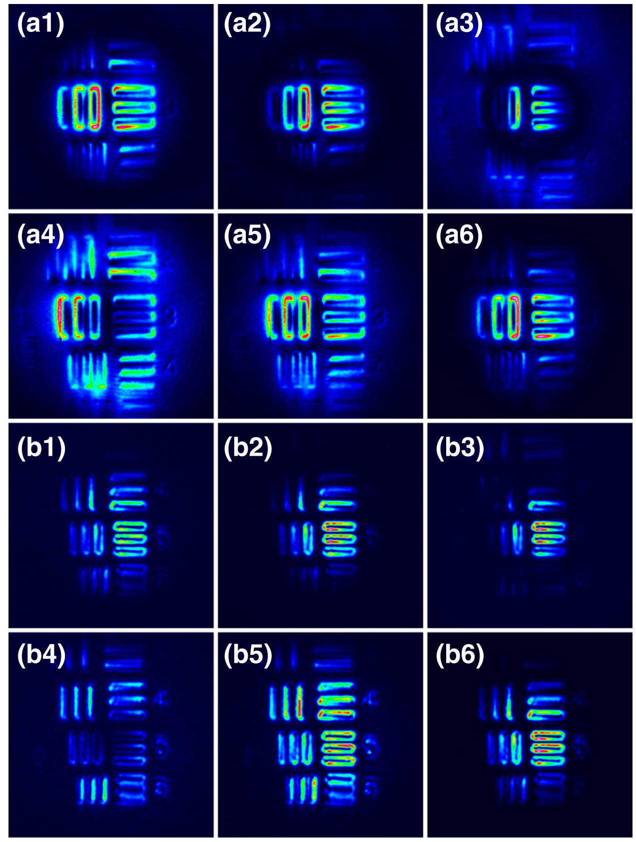

FIG. 5. Up-converted SPC images at different temperatures. Images (a1)–(a6) are acquired using configuration *A* and images (b1)–(b6) are acquired using configuration *B*. The temperature conditions for images (a1)–(a6) and images (b1)–(b6) are 18.7 °C, 24.1 °C, 29.6 °C, 34.5 °C, 37.1 °C, and 45.7 °C, respectively.

V. CONCLUSIONS

In summary, we first demonstrate two image processing methods that provide both FOV and edge enhancement separately and simultaneously via an up-conversion process using invisible illumination at around 1550 nm with two configurations. Comparatively speaking, configuration *B* offers the advantages of a more compact experimental set up, parallel processing, much lower background scattered noise, and a higher contrast radio. In other words, all processes, including frequency up-conversion, spiral phase contrast, and FOV enhancement, can be skillfully parallel processed in the nonlinear crystal in a single step because sum frequency generation acts as a natural multiplier of the two beams and significantly improves the processing efficiency. In addition, the imaging results in terms of both FOV and edge contrast are in good agreement with those of the simulations. Because the optical method has the advantages of parallel processing and high-speed operation, it may be applicable to real-time holographic displays via a spiral light modulator, which will provide the extra benefits of high flexibility and high resolution [25]. The up-conversion SPC imaging scheme presented here may also have direct applications in reagent-free biological imaging, pattern recognition, and edge detection in the near future. The flexibility and extensibility of the proposed experimental up-conversion set up will provide several potential choices to allow image processing based on multiple specific circumstances.

APPENDIX

We now provide the detailed method used for the imaging simulation that was mentioned above. The field distribution of light is expressed discretely using a matrix in MATLAB software. The two-valued function of the USAF-1951 resolution target is given as T. On the object plane, the field distribution is the product of the transverse distribution of a Gaussian beam and T, which can be written as

$$U_o = T\exp(-r^2/w_1^2), \tag{A1}$$

where $r=\sqrt{x^2+y^2}$ is the radial coordinate and w_1 is the radius of the beam waist. The propagation in the paraxial optical system of U_o is calculated using the Collins diffraction integral equation [26]

$$U_2 = \frac{1}{i\lambda B}\iint\limits_{\Sigma_1} U_1 e^{ikd+\frac{ik}{2B}[A(x_1^2+y_1^2)+D(x_2^2+y_2^2)-2(x_1x_2+y_1y_2)]}d\sigma_1, \tag{A2}$$

where U_1 is the input field and U_2 is the propagation result, d is the total length of the system, and A, B, C, and D are the elements of the ray transfer matrix ($ABCD$ matrix) of the system. $\sum_1$ is the plane of U_1. To obtain the field distribution in the crystal, we calculate the ray transfer matrix between the object plane and a specified plane in the crystal. The ray transfer matrix around a thin lens is given by

$$M_l(l_1,l_2) = \begin{pmatrix} 1-\frac{l_2}{F} & l_1 l_2\left(\frac{1}{l_1}+\frac{1}{l_2}-\frac{1}{F}\right) \\ -\frac{1}{F} & 1-\frac{l_1}{F}\end{pmatrix}, \tag{A3}$$

where l_1 and l_2 are the distances before and after the lens, respectively. Figure 6 shows the configuration B used in our experiment. For Lens1, $l_1 = F$ and $l_2 = F - L/2n_1$. The remaining part of the crystal should take the refractive index n_1 and the interface between the different refractive indices of the air and the crystal into account. We establish a coordinate system with the center of the crystal as the origin and set right as the positive direction. For a plane in the crystal with the coordinate z, the ray transfer matrix is expressed as shown below

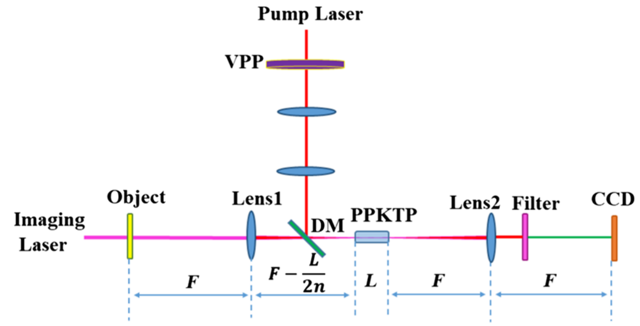

FIG. 6. Experimental set up of configuration B.

$$M_1 = M_c\left(n_1 z+\frac{n_1 L}{2}\right)M_i\left(\frac{1}{n_1}\right)M_l(l_1,l_2) = \begin{pmatrix}\frac{(1/n_1-1)L-2z}{2F} & F \\ -\frac{1}{n_1 F} & 0\end{pmatrix}, \tag{A4}$$

where $M_c(x) = \left(\begin{smallmatrix}1 & x\\ 0 & 1\end{smallmatrix}\right)$ is the propagation matrix in the crystal, $M_i(x) = \left(\begin{smallmatrix}1 & 0\\ 0 & x\end{smallmatrix}\right)$ is the matrix of the interface, and L is the length of the crystal. We then substituted $d = 2F + [(n_1 - 1)/2n_1]L + z$, $k = k_1 = n_1(2\pi/\lambda_1)$, $U_1 = U_o$, and the elements of M_1 into Eq. (2) to obtain $U_2(z) = A_1 e^{ik_1 z}$, which is the field distribution in the crystal. The amplitude is given by

$$A_1 = \frac{e^{ik_1\left(2F+\frac{n_1-1}{2n_1}L\right)}}{i\lambda F} \times \iint\limits_{S_1} U_o e^{\frac{ik_1}{2F}\left[\frac{(1/n_1-1)L-2z}{2F}(x_1^2+y_1^2)-2(xx_1+yy_1)\right]}d\sigma_1. \tag{A5}$$

In addition, the pump beam with OAM is approximated using the Laguerre-Gauss mode LG01 for simplicity as follows

$$A_2 = \frac{r}{[w_2(1+i\xi)]^2}e^{-\frac{r^2}{w_2^2(1+i\xi)}}e^{i\varphi}. \tag{A6}$$

Here, $\xi = 2z/k_2 w_2^2$, $k_2 = n_2(2\pi/\lambda_2)$, w_2 is the radius of the beam waist, and $\varphi = \arctan(y/x)$ is the angular coordinate. We then use the split-step Fourier method [27] to solve the coupled wave equation

$$i2k_3\frac{\partial A_3}{\partial z} + \nabla_\perp^2 A_3 = -\frac{\omega_3^2 d_{\text{eff}}}{\varepsilon_0 c^2}A_1 A_2 e^{i\Delta kz}, \tag{A7}$$

where $k_3 = n_3(2\pi/\lambda_3)$. To perform the numerical calculations, the propagation of the beam in the nonlinear crystal is divided into N steps. Then, the linear term and the nonlinear term are calculated separately in each step. The linear term is calculated using the following equation

$$dA_3(x,y,z) = \frac{i}{2k_3}\left(\frac{\partial^2}{\partial x^2}+\frac{\partial^2}{\partial y^2}\right)A_3(x,y,z)dz, \quad (A8)$$

where $dz = L/N$ is the length of a step. This equation can be solved using a two-dimensional Fourier transform. Here, we write the solution using the difference form for the numerical calculations.

$$\begin{aligned} dA_3 &= A_3(m+1) - A_3(m) \\ &= -\frac{i}{2k_3}F^{-1}\{(k_x^2+k_y^2)F[A_3(m)]\}dz, \end{aligned} \quad (A9)$$

where k_x and k_y are the transverse wave vectors. In addition, the nonlinear term is calculated using

$$dA_3 = A_3(m+1) - A_3(m) = \frac{i}{2k_3}\frac{\omega_3^2 d_{\rm eff}}{\varepsilon_0 c^2}A_1 A_2 e^{i\Delta kz}dz. \quad (A10)$$

The integration can be approximately solved step-by-step using the recurrence relation

$$\begin{aligned} A_3(m+1) = A_3(m) &+ \frac{i}{2k_3}\frac{\omega_3^2 d_{\rm eff}}{\varepsilon_0 c^2}A_1 A_2 e^{i\Delta kz}dz \\ &- \frac{i}{2k_3}\mathcal{F}^{-1}\{(k_x^2+k_y^2)\mathcal{F}[A_3(m)]\}dz, \end{aligned} \quad (A11)$$

where $m = 0, 1, 2, \ldots, N$ is the ordinal number of steps and $A(0) = 0$. The final result of the iteration is $A_3 = A(N)$.

After the nonlinear process, we substitute $d = 2F$, $k = 2\pi/\lambda_3$, and the elements of $M_2 = M_l(F,F)M_i[n(\lambda_3)]$ into Eq. (A2) to obtain the field distribution in the image plane. In the code, we directly change the parameter Δk to simulate the FOV enhancement.

In the above simulation, we use the following parameters:$w_1 = 1, w_2 = 1$, $N = 20$. We find that a larger w_2 value leads to clearer image edge enhancement. We, therefore, condense the parallel pump beam rather than focus it in our experiments. One point that should be considered in the FOV enhancement simulation is that the Δk corresponding to a certain effect is not precise and varies with N. To avoid this phenomenon, we provide an approximate calculation that can explain the FOV enhancement to a certain extent. We introduced the numerical calculation above. Here, we analytically solve Eq. (A7) in the plane wave approximation. Equation (A7) can be simplified to read

$$i2k_3\frac{\partial A_3(x,y,z)}{\partial z} = -\frac{\omega_3^2 d_{\rm eff}}{\varepsilon_0 c^2}A_1(x,y,z)A_2 e^{i\Delta kz}, \quad (A12)$$

where we also assume approximately that $A_2 \equiv \exp(i\varphi - r^2/w_2^2)$ in the thin crystal. Therefore, we obtain the following equation

$$A_3 = i\frac{\omega_3^2 d_{\rm eff}}{2k_3\varepsilon_0 c^2}e^{i\varphi-\frac{r^2}{w_2^2}}\int_{-L/2}^{L/2}A_1 e^{i\Delta kz}dz. \quad (A13)$$

We then substitute Eq. (A5) into Eq. (A13) and obtain

$$\begin{aligned} A_3(x,y) = \frac{\omega_3^2 d_{\rm eff} e^{-\frac{r^2}{w_2^2}+i\varphi}}{2k_3\varepsilon_0 c^2\lambda_1 F}\iint_{S_1}\operatorname{sinc}\left[\frac{L}{2}\left(\Delta k - \frac{k_1(x_1^2+y_1^2)}{2F^2}\right)\right] \\ \times U_o(x_1,y_1)e^{ik_1\frac{(1/n_1-1)L}{4F^2}(x_1^2+y_1^2)}e^{i\frac{k_1}{F}(-xx_1-yy_1)}d\sigma_1. \end{aligned} \quad (A14)$$

This equation can be regarded as a two-dimensional Fourier transform, where $\exp[i(k_1/F)(-xx_1 - yy_1)]$ is the kernel of the transform. In addition, Lens2 can be regarded as another Fourier transform of the field, thus meaning that the field distribution in the image plane is

$$\begin{aligned} U_i = \mathcal{F}\{A_3\} \propto \mathcal{F}\left\{e^{-\frac{r^2}{w_2^2}+i\varphi}\right\} * \left\{T(-\alpha x, -\alpha y)e^{-\frac{\alpha^2 r^2}{w_1^2}}\right. \\ \left. \times\operatorname{sinc}\left[\frac{L}{2}\left(\Delta k - \frac{k_1\alpha^2 r^2}{2F^2}\right)\right]e^{ik_1\frac{(1/n-1)L}{4F^2}\alpha^2 r^2}\right\}, \end{aligned} \quad (A15)$$

where $\alpha = \lambda_1/n_1 n_3 \lambda_3$ is the zooming factor. This equation can explain both the SPC effect and the FOV enhancement. In addition to the Gaussian factor, the object T is also modulated using a sinc function factor with variable Δk, which is caused by the nonlinear process. This sinc function reaches a maximum value when the argument is zero. Therefore, the position of the relative maximum of the field changes with increasing Δk. Additionally, we can also see that the SPC and FOV enhancement make contact with each other via the linear convolution operation. The two effects are thus approximately independent of each other.

ACKNOWLEDGMENTS

Funding: National Natural Science Foundation of China (NSFC) (Grants No. 61435011, No. 61525504, and No. 61605194); Anhui Initiative in Quantum Information Technologies (Grant No. AHY020200**)**, the China Postdoctoral Science Foundation (Grant No. 2016M590570), and the Fundamental Research Funds for the Central Universities.

[1] Uday K. Tirlapur and Karsten König, Targeted transfection by femtosecond laser, Nature **418**, 290 (2002).
[2] S. Gioux, H. S. Choi, and J. V. Frangioni, Molecular imaging agents specific for the annulus fibrosus of the intervertebral disk, Mol. Imaging **9**, 7290 (2010).
[3] R. Hudson and J. Hudson, The military applications of remote sensing by infrared, Proc. IEEE **63**, 104 (1975).
[4] C.-L. Wang, X.-D. Mei, L. Pan, P.-W. Wang, W. Li, X. Gao, Z.-W. Bo, M.-L. Chen, W.-L. Gong, and S.-S. Han, Airborne near infrared three-dimensional ghost imaging LiDAR via sparsity constraint, Remote Sens. **10**, 732 (2018).
[5] A. P. Vandevender and P. G. Kwiat, High efficiency single photon detection via frequency up-conversion, J. Mod. Opt. **51**, 1433 (2004).
[6] A. J. Torregrosa, H. Maestre, and J. Capmany, Intra-cavity upconversion to 631 nm of images illuminated by an eye-safe ASE source at 1550 nm, Opt. Lett. **40**, 5315 (2015).
[7] F. Zernike, Phase contrast, a new method for the microscopic observation of transparent objects, Physica **9**, 686 (1942).
[8] S. Fürhapter, A. Jesacher, S. Bernet, and M. Ritsch-Marte, Spiral phase contrast imaging in microscopy, Opt. Express **13**, 689 (2005).
[9] A. Jesacher, S. Fürhapter, S. Bernet, and M. Ritsch-Marte, Shadow Effects in Spiral Phase Contrast Microscopy, Phys. Rev. Lett. **94**, 233902 (2005).
[10] J.-K. Wang, W.-H. Zhang, Q.-Q. Qi, S.-S. Zheng, and L.-X. Chen, Gradual edge enhancement in spiral phase contrast imaging with fractional vortex filters, Sci. Rep. **5**, 15826 (2015).
[11] B. Jack, J. Leach, J. Romero, S. Franke-Arnold, M. Ritsch-Marte, S. M. Barnett, and M. J. Padgett, Holographic Ghost Imaging and the Violation of a Bell Inequality, Phys. Rev. Lett. **103**, 083602 (2009).
[12] M. Ritsch-Marte, Orbital angular momentum light in microscopy, Philos. Trans. R. Soc. Lond. A **375**, 20150437 (2017).
[13] J. Nee, R. McCanne, K. Kubarych, and M. Joffre, Two-dimensional infrared spectroscopy detected by chirped-pulse upconversion, Opt. Lett. **32**, 713 (2007).
[14] G. Gibson, B. Sun, M. Edgar, D. Phillips, N. Hempler, G. Maker, G. Malcolm, and M. Padgett, Real-time imaging of methane gas leaks using a single-pixel camera, Opt. Express **25**, 2998 (2017).
[15] C. Corsi, Infrared: A key technology for security systems, Adv. Opt. Technol. **2012**, 838752 (2012).
[16] A. M. Hanninen, R. C. Prince, R. Ramos, M. V. Plikus, and E. O. Potma, High-resolution infrared imaging of biological samples with third-order sum-frequency generation microscopy, Opt. Express **9**, 4807 (2018).
[17] R. Demur, R. Garioud, A. Grisard, E. Lallier, L. Leviandier, L. Morvan, N. Treps, and C. Fabre, Near-infrared to visible upconversion imaging using a broadband pump laser, Opt. Express **26**, 13252 (2018).
[18] H. Maestre, A. J. Torregrosa, and J. Capmany, IR image upconversion under dual-wavelength laser illumination, IEEE Photonics J. **8**, 1 (2016).
[19] S. Junaid, J. Tomko, M. P. Semtsiv, J. Kischkat, W. T. Masselink, C. Pedersen, and P. Tidemand-Lichtenberg, Mid-infrared upconversion based hyperspectral imaging, Opt. Express **26**, 2203 (2018).
[20] H. Maestre, A. J. Torregrosa, C. R. Fernández-Pousa, and J. Capmany, IR-to-visible image upconverter under nonlinear crystal thermal gradient operation, Opt. Express **26**, 1133 (2018).
[21] X.-D. Qiu, F.-S. Li, W.-H. Zhang, Z.-H. Zhu, and L.-X. Chen, Spiral phase contrast imaging in nonlinear optics: seeing phase objects using invisible illumination, Optica **5**, 208 (2018).
[22] M. Pierrou, F. Laurell, H. Karlsson, T. Kellner, C. Czeranowsky, and G. Huber, Generation of 740 mW of blue light by intracavity frequency doubling with a first-order quasi-phase-matched KTiOPO4 crystal, Opt. Lett. **24**, 205 (1999).
[23] Z.-Y. Zhou, Y. Li, D.-S. Ding, Y.-K. Jiang, W. Zhang, S. Shi, B.-S. Shi, and G.-C. Guo, Generation of light with controllable spatial patterns via the sum frequency in quasi-phase matching crystals, Sci. Rep. **4**, 5650 (2014).
[24] Marshall J. Cohen and Gregory H. Olsen, in SPIE 1946, Infrared Detectors and Instrumentation (1993).
[25] F. Yaraş, H. Kang, and L. Onural, Real-time phase-only color holographic video display system using LED illumination, Appl. Opt. **48**, H48 (2009).
[26] H. T. Yura and S. G. Hanson, Optical beam wave propagation through complex optical systems, JOSA A **4**, 1931 (1987).
[27] P. L. Stoffa, J. T. Fokkema, R. M. de Luna Freire, and W. P. Kessinger, Split-step Fourier migration, Geophysics **55**, 410 (1990).